Surface circulation characterization along the middle-south coastal region of Vietnam from high-frequency radar and numerical modelling

Thanh Huyen Tran[1,2], Alexei Sentchev[1], Duy Thai To[3], Marine Herrmann[4], Sylvain Ouillon[2,4], Kim Cuong Nguyen[5]

[1] Laboratory of Oceanology and Geosciences (LOG), UMR 8187, Univ. Littoral Côte d'Opale, CNRS, Univ. Lille, IRD, Wimereux, France
[2] Land-Ocean-Atmosphere Regional Coupled System Study Center (LOTUS), University of Science and Technology of Hanoi (USTH), Hanoi, Vietnam
[3] Institute of Oceanography, Vietnam Academy of Science and Technology (VAST), Nha Trang, Vietnam
[4] Laboratory of Space Geophysical and Oceanographic Studies (LEGOS), UMR 5566, IRD, CNES, CNRS, UPS, Toulouse, France
[5] University of Science (HUS), Vietnam National University, Hanoi, Vietnam

Correspondence to: huyen-thanh.tran@univ-littoral.fr

Abstract. Coastal water dynamics along the Vietnam Middle-South Coastal region (VMSC), part of the South China Sea, is highly complex with large spatio-temporal variability whose drivers are not yet well understood. For the first time, high-resolution surface current data from high-frequency radar (HFR) measurements were obtained in this region during the early (transition) phase of the Asian summer monsoon. The data were used to compare with simulation results from a circulation model, SYMPHONIE, and ultimately to optimise the wind forcing in the model. Both modelling and HFR were able to show the spatial and temporal evolution of the surface circulation, but some discrepancies were found between model and HFR data on some days, coinciding with the evolution of the wind. Two methods were used to optimise the wind forcing, namely the Ensemble Perturbation Smoother (EnPS) and the wind correction method using wind-driven surface currents (EkW). Both methods achieved a significant reduction (~36-40 %) in the error of the surface current velocity fields compared to the measured data. Optimised winds obtained from the two methods were compared with satellite wind data for validation. The results show that both optimisation methods performed better in the far field, where topography no longer affects the coastal surface circulation. The optimisation results revealed that the surface circulation is not only driven by winds but also by other factors such as intrinsic ocean variability which is not entirely controlled by boundary conditions. This indicates the potential usefulness of large velocity datasets and other data fusion methods to effectively improve modelling results.

1 Introduction

The coastal waters of Vietnam are parts of the South China Sea (SCS) ("East Sea" in Vietnamese term), one of the world's largest marginal seas, where various meteorological and oceanographic processes contribute to its circulation variability at

different scales. The region is under the influences of two monsoonal wind regimes: the southwest monsoon usually starts from June while the northeast wind usually begins from late November and is fully developed in January (Potemra and Qu, 2009; Wang et al., 2021). The large scale circulation in the SCS is mainly driven by winds (Potemra and Qu, 2009), resulting in seasonal patterns and phenomena which have been documented in many studies: SCS western boundary current (Fang et al., 2012), a dipole structure characterized by cyclonic and anti-cyclonic gyres offshore Vietnam (Chen et al., 2012; To Duy et al., 2022; Wang et al., 2006), and a South Vietnam upwelling (SVU) which usually occurs in summer (Chen et al., 2012; Da et al., 2019; To Duy et al., 2022; Herrmann et al., 2023, 2024). In particular, along the middle-south coasts of Vietnam (hereafter called VMSC), shown in Fig. 1b, all the three features of circulation mentioned above are present. Besides, the coastal dynamics along the VMSC is strongly influenced by ocean intrinsic variability (OIV): producing variations of upwelling expansion, location of current jets, sub-mesoscale eddies - their intensity and size (Li et al., 2014; To Duy et al., 2022; Da et al., 2019; Herrmann et al., 2023). These findings have emphasized that the dynamics of the VMSC is highly complex with large space and time variability governed by different factors, which are still not well understood.

The limitation of existing studies in the SCS, in particular along the VMSC, is that their research mostly relied on coarse-resolution modelling, intermittent satellite data and discrete measurements. Furthermore, it is worth noting that, the majority of recent studies in the region mainly focused on the ocean dynamics and circulation variability during the matured monsoon periods, meanwhile, ocean dynamics during the transition periods is still lacking of knowledge. During the transition period, the wind changes direction in complex ways thus affecting the temporal and spatial variability of the surface currents. These, among others, can generate various dynamic structures i.e. submeso-scale eddies, divergence and convergence zones. Modelling approach, to some extents, can help to acquire a general understanding of the ocean circulation with sufficient and reliable forcing inputs. However, for Vietnam coastal regions, atmospheric forcing data, especially winds, are very limited and often come from global data sources with low spatial resolution, thus, some dynamic features at local/regional scales can be poorly presented or even neglected. Nguyen-Duy et al. (2023) have conducted sensitivity tests of Red River plume dynamics to wind fields in the Gulf of Tonkin. The river plume was found to be sensitive to wind variations which generate a clear reversal of the circulation pattern and affect the plume thickness variability. Meanwhile, as was demonstrated in our preliminary work, during the transition period of the summer monsoon from April to May, the VMSC coastal dynamics experienced a high variability both in terms of temporal and spatial scales associated with large variability in wind fields (Tran et al., 2022). Thus, in order to deliver a comprehensive understanding of the coastal dynamics during the monsoonal transition period, high-resolution datasets and better, reliable model simulation results are necessary.

The questions now are, how high-resolution measurements can be used and how numerical models can be improved for better simulating fine-scale processes in coastal regions, in particular, along the VMSC? In the past years, drifters and satellite-derived data have been used in many studies as the sources of observation data. Centurioni et al. (2009) used Surface Velocity Program drifters with reanalysis wind and satellite altimetry data to construct 2D circulation maps in the SCS at 1° resolution. Similar approach has been employed for estimating mean geostrophic currents in the SCS with Argo profiling floats and altimeter data (Yang et al., 2019; Zhou et al., 2010). Nonetheless, these products only provide estimated or derived sea surface

currents (SSC). Up-to-now, no direct measurements with high-spatio-temporal resolution are available for the VMSC. High-frequency radar (HFR), a land-based remote sensing technique, has been widely used in oceanographic studies since the system has the ability to monitor SSC directly with high temporal and spatial coverage (Mantovani et al., 2020). The capability of HFRs in monitoring surface currents in the tropic coastal regions have been proven in a number of existing studies within a

70 wide range of oceanographic applications, e.g. coastal circulation characterization (Cosoli et al., 2020), assessing the turbulence dispersion of passive tracers and particulate materials (Tran et al., 2022), and coastal circulation response to climatic variabilities (Gu and Mao, 2024). On the Vietnam coasts, two different radar systems have been installed: three CODAR Seasondes at ~6km resolution in the Gulf of Tonkin, north of the SCS (Rogowski et al., 2019); and two WavE RAdars (WERA) at 1km resolution in the VMSC. Our preliminary results showed that HFRs could demonstrate well the fine-scale structure of

75 coastal circulations during the transition monsoon period (Tran et al., 2022). In terms of modelling, in the most recent studies of Herrmann et al., (2023, 2024); To Duy et al., (2022), high-resolution circulation model SYMPHONIE was used to investigate the interannual variabilities of SVU in the SCS including the VMSC. However, no current velocity measurements have been used for model validation or optimization.

There are several approaches in model forcing optimization, for example, correcting the model boundary conditions (tides and

80 winds). In this method, sets of perturbed wind and tidal forcing ensembles were generated with inverse Fast Fourier Transform (FFT) method. Subsequently, tidal and wind forcing were optimized via data assimilation techniques (Barth et al., 2009, 2011; Marmain et al., 2014). In the Gulf of Tonkin, European Center for Medium-Range Weather Forecasts (ECMWF) wind forcing was perturbed by using Empirical Orthogonal Functions (EOF) analysis for model cluster analysis (Nguyen-Duy, 2022). Differing from these two methods, our research introduces a physical approach which quantifies the surface current component

85 induced by winds using HFR data, without ensemble simulation. The method allows to optimize the wind forcing input of the 3D-ocean circulation model SYMPHONIE with the expectation to improve the capabilities of the model in simulating fine-scale coastal current structures of the VMSC during the onset of the summer monsoon.

2 Methodology

2.1 HFR measurements in the VMSC region

90 HFR system used in the study is a pair of WERA ocean radars with the central operating frequency of 16.15MHz. Radial surface current velocities were measured by two radar stations (denoted as V1, V2 in Fig. 1c) during the measurement campaign in Phu Yen, VMSC from 14th of April to 16th of May, 2019. The measurement domain spanned from [12° 53' N, 109° 16' E] to [13° 22' N, 109° 47' E] with a spatial resolution of 1km. The raw radial velocities were treated with RMSE-threshold filtering in order to be free of spikes. Surface current velocity vectors were then reconstructed from the noise-

95 removed radial velocities with the 2DVar/EOF method (Yaremchuk and Sentchev, 2009, 2011). The interpolation and gap filling procedure has been explained in our previous work (Tran et al., 2022).
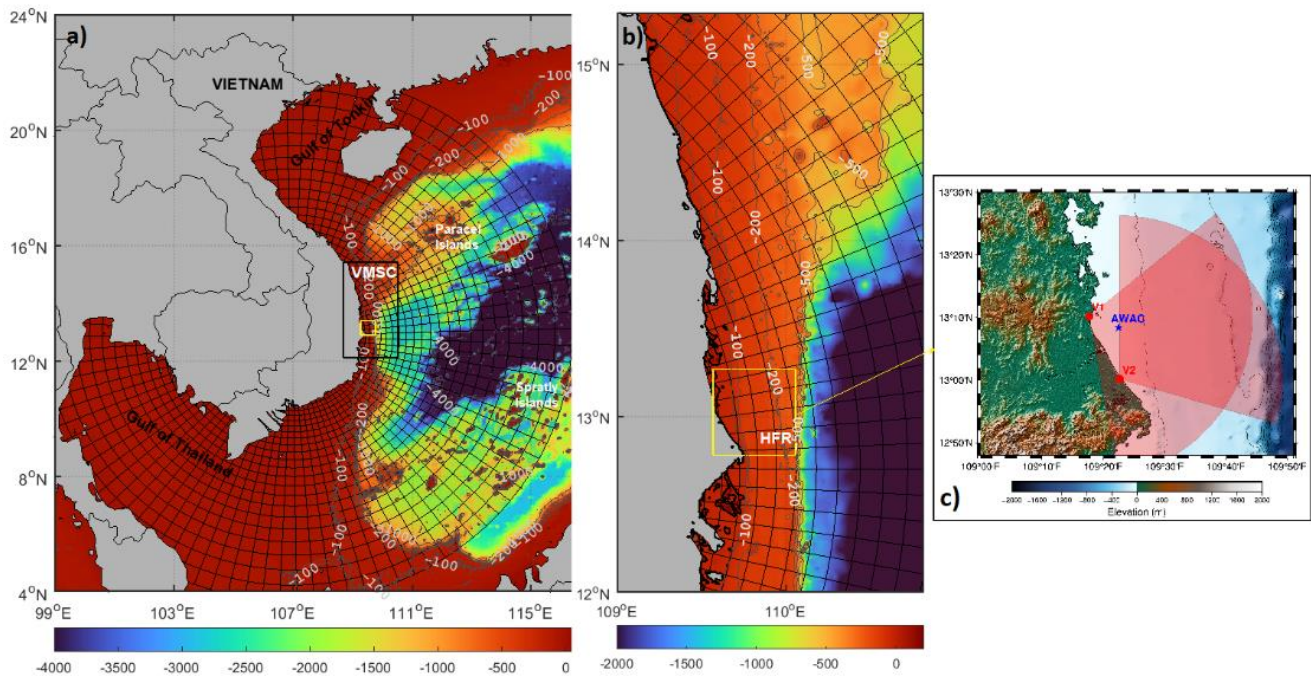
Figure 1: a) Bathymetry map of the EASTSEA domain and b) the VMSC domain (right) (bathymetry data source: GEBCO_2022). VMSC domain is bounded with black box, HFR domain bounded with yellow box. The computation orthogonal curvilinear grid is illustrated by black solid curves (the grid node density was reduced for better demonstrative purpose); c) Spatial coverage by WERA radars installed in April-May 2019 at the Phu Yen coasts, VMSC. Red dots show the two HFR stations V1, V2. Blue star shows location of AWAC. Bathymetry contours are shown by black solid lines.

The surface currents derived from the HFR data have been validated with 7-day surface current velocity measurements obtained from a bottom-mounted AWAC (Acoustic Wave And Current Profiler) during April 16-22, 2019. The velocity time series from HFR measurements has been extracted at grid cell in closest proximity to the AWAC location.

Three metrics of evaluation have been used to compare the current velocity time series from AWAC and HFR: correlation (R), root-mean-squared error (RMSE) and mean absolute error (MAE) of surface current velocities. The results show that velocity time series obtained from HFR and AWAC were in a fairly good agreement (R=0.58, RMSE=0.10 ms^{-1}, MAE=0.07 ms^{-1} for u- and R=0.72, RMSE=0.13 ms^{-1}, MAE=0.11 ms^{-1} for v-components) (Fig. 2). The discrepancy between the two velocity time series may be attributed primarily to the velocity shear affecting the surface layer and different depths of AWAC and HFR measurements. AWAC velocities were recorded and averaged in the 1.5 m depth layer (the bin size), closest to the sea surface. Meanwhile, the effective depth of HF radar at 16.15 MHz was determined to be 0.74 m. Besides, Fig. 2 clearly shows the impact of surface waves and tidal stage, contaminating AWAC measurements, particularly during the peak flow.
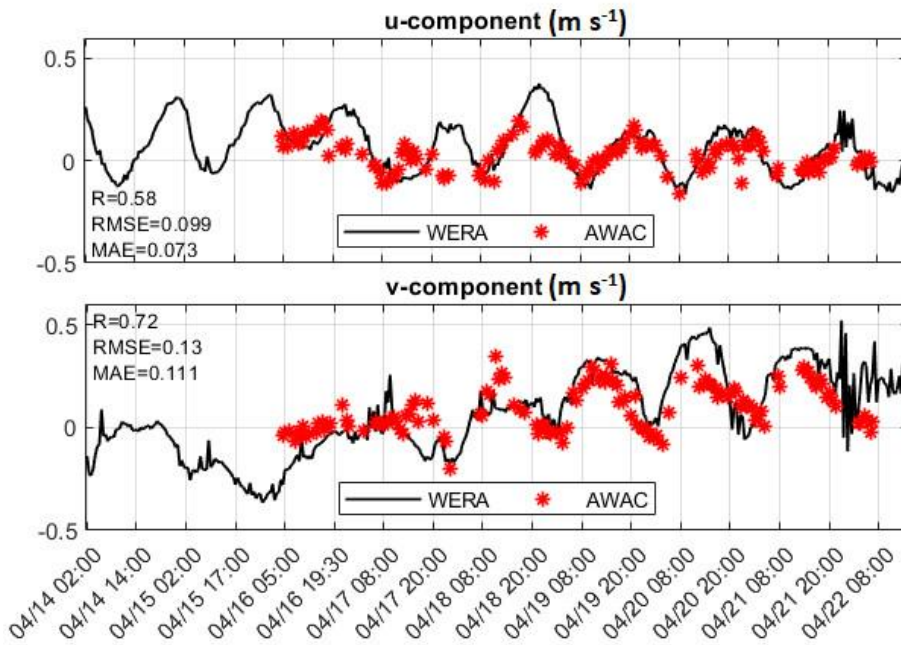
4

Figure 2: Comparison of SSC time series from HFR (black solid line) and AWAC (red asterisk points)

2.2 3D-circulation model SYMPHONIE

The 3D ocean circulation model SYMPHONIE is a Boussinesq hydrostatic ocean circulation model developed by the
120   SIROCCO group (CNRS & Toulouse University, France). Based on an Arakawa curvilinear C-grid, momentum and tracer
fluxes are computed using an energy conserving finite difference method (Marsaleix et al., 2008). The model adopts the time
stepping method, using Leap Frog scheme combined Laplacian filter; K-epsilon turbulence closure scheme, and pressure
gradient Jacobian scheme to describe the physics within the model. Description of various boundary conditions including
lateral open boundaries, rivers, surface conditions can be found in (Estournel et al., 2009).
125   The model configuration used in this research was adopted from the regional model configuration described and used in Duy
et al., (2022); Herrmann et al., (2023, 2024); and Trinh et al., (2024) . The grid resolution is ~1 km nearshore and coarsens
gradually to ~4.5 km in the open seas. The atmospheric forcing is introduced via the bulk formulae of Large and Yeager (2004)
using the 3-hourly output of the ECMWF 1/8º atmospheric analysis. Initial ocean conditions and lateral ocean boundary
conditions are prescribed from the daily outputs of the global ocean 1/12º analysis PSY4QV3R1 from the Copernicus Marine
130   and Environment Monitoring Service (CMEMS). Tidal data were taken from the 2014 release of the finite-element solution
(FES2014) global tidal model. Nine tidal constituents have been taken into account. River forcing was enabled with the
information of river systems along the coasts and was described in To Duy et al. (2022).
The model domains are shown in Fig. 1. The first simulation started from January to June, 2019 on the entire SCS domain
(Fig. 1a) (EASTSEA run) in order to obtain open boundary conditions (OBC) for the VMSC domain (Fig. 1b). The second

135 simulation (VMSC run) has been conducted in the VMSC domain from March 1 to May 5, 2019 for generating initial conditions before the optimization procedure was executed. The VMSC domain has the same grid resolution as the EASTSEA domain. Details of the experiment setup are described in Sect. 2.4.

2.3 Methods of wind forcing optimization

2.3.1 Ensemble perturbation smoother (EnPS)

140 The wind optimization procedure adopted from (Barth et al., 2011; Marmain et al., 2014) consists of two steps: (1) ensemble perturbation and (2) data assimilation.

A total of 30 ensembles were generated during a period of two months (April-May, 2019) by using wind fields with perturbation data.

The perturbations ($w_p(x, y, t)$) were computed from the real part of a quantity which are the sum of the multiplication of a
145 random complex normal-distribution time-series ($z_k(t)$) and decomposed wind fields ($a_k(x, y)$) obtained from Fast Fourier Transform (FFT):

$$w_p(x, y, t) = \alpha \, \text{Re}\left(\sum_{k=1}^{N} a_k(x, y) \, z_k(t)\right) \tag{1}$$

N is the total time-series length of wind data during the two months. α is the scaling factor between the final expected wind error and temporal error. With this method of perturbation, the spatial and temporal distributions of wind perturbation errors
150 were assumed to be similar to that of ECMWF winds in order to avoid errors induced by nonlinear variabilities.

EnPS is a non-sequential method where all observations are used to generate optimal state (an analysis) for a specific DA time window. The analysis of wind w^a is yielded from the equation:

$$w^a = w^b + w^{incr}, \tag{2}$$

where w^b is the background wind, w^{incr} is the increment added to the background field. This increment can be achieved from
155 the relationship of a number of quantities: the covariance matrix of wind ensembles (**S**), the covariance matrix of so-called "observation operators" that link model surface currents with wind forcing (**E**), the observation error matrix **R**, and the difference between observations y^o and the model operators $h(w^b)$. Hence, the Eq. (2) can be rewritten as:

$$w^a = w^b + \mathbf{SE}^T(\mathbf{EE}^T + \mathbf{R})^{-1}(y^o - h(w^b)), \tag{3}$$

in which, $\mathbf{SE}^T$ represents the covariance matrix between wind forcing and model (surface currents), while the covariance
160 matrix of model surface currents is represented by $\mathbf{EE}^T$:

$$\mathbf{SE}^T = cov\left(w^b, h(w^b)\right) \tag{4}$$

$$\mathbf{EE}^T = cov\left(h(w^b), h(w^b)\right) \tag{5}$$

The detailed explanation of the DA scheme and the components of the formula can be found in Barth et al. (2009, 2011).

In this research, we conducted DA for a 10-day long analysis period (May 5-14, 2019) with a time window of 24-hours. For each DA run, 8 instances of wind data (3h interval) corresponding to 24 instances of surface current data (1h interval) were used.

2.3.2 Wind correction from wind-driven surface currents (EkW)

We assume that the uncertainty of model surface current simulation comes only from the inaccuracy of wind forcing without consideration of other sources of uncertainties (i.e. open boundary conditions, initial conditions and other forcing fields). In other words, the wind-driven component of surface currents was not properly reproduced in the model due to coarse-resolution wind data. This uncertainty can be compensated by a correction of model surface currents $(\boldsymbol{u}_{cor})$ represented by the difference between observations, i.e., surface currents obtained from HFR $(\boldsymbol{u}_R)$ and model $(\boldsymbol{u}_M)$:

$$\boldsymbol{u}_{cor} = \boldsymbol{u}_R - \boldsymbol{u}_M \tag{6}$$

For each value of wind data, surface currents at neighbouring points located within a certain distance R to the wind data point were considered. In order to validate the method later with the same measurement data from HFR, only 60 % of the data points in HFR current field were randomly selected for the wind forcing correction. The remaining 40 % of data were used for evaluation of the optimization method skill.

We quantified the contribution of the sea state (surface waves) to the surface current obtained from HF radar using equations A4 and A5 in the paper of Sentchev et al., (2013). The contribution of Stokes-drift to the total velocity measured by HF radar was estimated at a maximum of around 4-5 % of the velocity value, i.e. at a maximum 0.02 ms^{-1}.

Due to the insignificant contribution of the wave-induced velocity component, it can be neglected when estimating wind-induced velocity, which is assumed to make the main contribution to the discrepancy between model and radar velocity. The correction of wind speed $\boldsymbol{w}_{cor}$ then could be estimated from the surface current velocities using the empirical formula of (Weber, 1983):

$$|\langle \boldsymbol{u}_{cor}(x_i, y_i, t) \rangle| \approx 27 \sqrt{C_d \frac{\rho_a}{\rho_0}} |\boldsymbol{w}_{cor}(x, y, t)| = \beta |\boldsymbol{w}_{cor}|, \tag{7}$$

where $C_d = 1.6 \times 10^{-3}$ is a constant drag coefficient, ρ_a and ρ_0 are the air and water densities respectively, and $\langle \boldsymbol{u}_{cor}(x_i, y_i, t) \rangle$ indicates the spatial average of velocities over a circular area with a radius R = 13 km (~0.125 degree).

As the temporal and spatial resolution of wind and surface current velocities are different, we applied a least-squares method to calculate 3h analysis wind from a series of 1h surface current velocities. The cost function in least-squares method is henceforth described in the following equation:

$$J(\boldsymbol{w}_{cor}) = (\langle H(\boldsymbol{u}_R - \boldsymbol{u}_M) \rangle - \beta \boldsymbol{w}_{cor})^2 \rightarrow min \tag{8}$$

Here, H is an operator projecting the current velocities in locations (x_i, y_i) onto the wind vector location.

The corrections of wind were finally added to the background wind field to obtain the analysis wind as in Eq. (2) of the EnPS method.

2.4 Experiment design

Since the focus of the paper is the VMSC region, we implemented the optimization steps only for the VMSC domain in order to reduce the cost of computation. The period chosen for model optimisation spanned from 5 to 14 May 2019. This period was featured by a significant change in wind direction resulted in a notable discrepancy between the velocities from model and HFR. A more detailed description of the analysed period can be found in Sect. 3.3. Before conducting optimization procedure, OBC and initial states of the model have to be generated. The first simulation was made for the entire EASTSEA domain to obtain OBC for the VMSC domain. Subsequently, initial states were created from the VMSC run. Three simulations, VMSC_ref, VMSC_EkW and VMSC_EnPS, used the same initial states provided by the VMSC run on May 5, 2019, but with three different wind forcing conditions (Table 1).

Table 1: Model run description

Model run	Period	Description
EASTSEA	Jan 1-June 1, 2019	Generate OBC for VMSC domain
VMSC	Mar 1-May 5, 2019	Spin-up run for OBC to be propagated into the VMSC domain
VMSC_ref	May 5-May 14, 2019	Reference run (free run)
VMSC_EkW	May 5-May 14, 2019	Simulation with EkW method
VMSC_EnPS	May 5-May 14, 2019	Simulation with EnPS method

Skills of the two optimization methods were evaluated by using RMSE and MAE of surface currents to compare the remaining 40% of the HFR measurement data with modelling results at corresponding point locations. For validating the performance of the two optimisation methods, wind data from Advanced Scatterometer Data Products (ASCAT) at 0.25-degree resolution were used to compare with EnPS and EkW wind data.

3 The VMSC hydrodynamics characterization during the monsoon transition period (April-May)

3.1 Spectral analysis

Spatially-averaged power spectral density (PSD) has been computed for the surface current velocity time-series obtained from HFR and VMSC_ref as well as for the wind velocity time-series from ECMWF during the measurement period (Fig. 3). In all cases, the power spectra have a similar shape for both cross-shore and along-shore dimensions. There are two prominent peaks in PSD of wind associated with inertial and diurnal periods. The diurnal cycle of winds is governed by the difference in surface

heating between land and sea, which leads to thermal exchanges and generates a sea breeze. Besides, a peak at 0.08 h^{-1} (12h period) observed in the PSD curve accounts for semi-diurnal variability of wind, which was also well reproduced in ECMWF wind data. This variability can result from the modulation of atmospheric circulation by tides and gravitational waves (Wu et al., 2022). Regarding PSD of current velocity, a frequency of ~0.04 hour^{-1} (24 h period) associated with diurnal tidal motions are found in both VMSC_ref and HFR, however, the level of energy differs considerably between the two time series. Lower-frequency band processes were also detected during this period of analysis including inertial motion caused by Coriolis force. Regarding the inertial period, a significant peak was found for VMSC_ref's time-series associated with wind time-series, but not for HFR measurements. The energy levels of VMSC_ref and HFR power spectra are comparable in the low frequency band until approximately 0.025 hour^{-1} (~40 h period) then the energy in VMSC_ref's power spectra declines drastically in high-frequency band compared to that in HFR measurement. Meanwhile, on the left side of the spectra, there are some slight shifts at longer periods (more than 1.5 days) between along-shore and cross-shore spectra. At synoptic scale (several days), wind and HFR spectra have a peak at a frequency band of approx. 0.0095 hour^{-1} (4-5 days), however the process in surface current show to be more resistant (wider peak) in time compared to that of wind (sharper peak). This pattern is not clearly observed in the spectrum of VMSC_ref's current velocity.
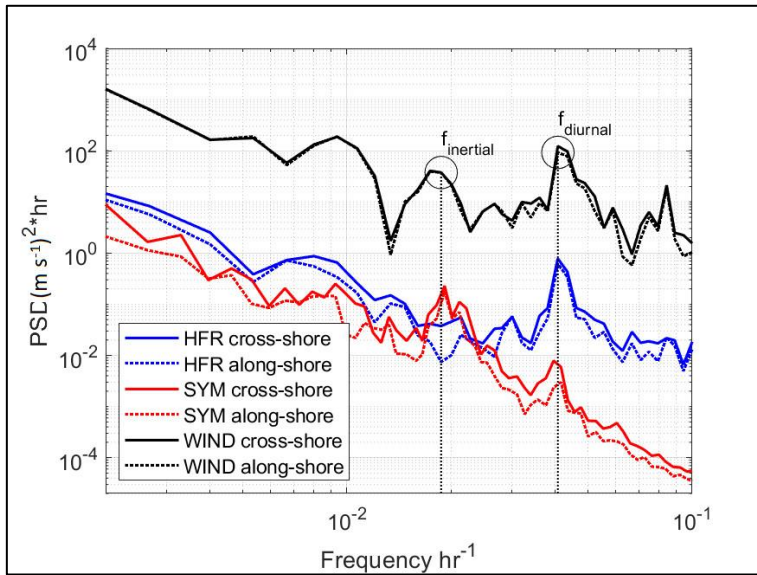

Figure 3: Power spectral density (PSD) of ECMWF wind velocity (black), SSC velocities from HFR (blue) and VMSC_ref (red)

In contrast to the PSD spectra of VMSC_ref's SSC, which show a clear energy cascade from larger to smaller scales, the steep slope in the high-frequency band (less than 24h period) is not visible for wind speed and velocity obtained from HFR measurements. The processes that govern wind variability operate on different scales compared to oceanic processes. In the sub-inertial band, the power-law scaling for wind (depicted by the black curves in Fig. 3) exhibits a slope close to -1, which

provides an indication of the wall turbulence (David S-K. Ting, 2016; Sim et al., 2023). In this specific case, the wind variability is significantly influenced by the characteristics of the surrounding terrain (Sim et al., 2023). In the case of currents, the flattening of the PSD curve in the sub-diurnal frequency band is likely attributable to noise affecting HFR data and the accuracy of current vector reconstruction from HFR measurements at two sites. Figure A1 in the Appendix illustrates a relatively high level of noise, at mid and far ranges of the radar coverage, that was induced by the power supply. In addition, the semi-diurnal peak ($0.08\ \text{h}^{-1}$) is present in HFR spectra but is not statistically significant due to its submergence in the noise. However, this peak is absent in the model spectra. One potential explanation is that the low-resolution forcing data used in the model simulation prevents the reconstruction of higher-frequency variabilities of surface circulation. A similar situation has been documented in previous studies from Cosoli et al., (2013) and Lauton et al., (2023). Their findings indicated that the model exhibited a strong coherence with observations in the low-frequency band. However, this was not the case in the high-frequency band.

3.2 Tidal analyses

The tidal components of surface currents were estimated for the measurement period using "Unified Tidal Analysis and Prediction" Matlab functions (Utide) developed by the University of Rhode Island (Codiga, 2011). The tidal regime in the region is predominately diurnal with three main tidal constituents: K1, P1 and O1. There are some differences in tidal ellipse spatial distributions between VMSC_ref and HFR. The HFR tidal ellipse maps show that clockwise rotation ellipses are observed near the coast, whereas counter-clockwise ellipses are located offshore and in the southeastern part of the domain. The shape of ellipses is more circular nearshore and more elongated seaward. The velocity magnitude is also larger offshore than nearshore (Fig. 4).

Meanwhile, this elongation of ellipses offshore is not visible in VMSC_ref. The magnitude of tidal currents from VMSC_ref is overall smaller than that from HFR. The better agreements between VMSC_ref and HFR are found in the middle field of the HFR domain (13-13.2º N, 109.4-109.6º E). Figure A1 in Appendix shows that higher uncertainties of both u- and v-components of SSC from HFR measurements are found in the offshore range starting from a distance of ~40 km. This pattern coincides with the discrepancies in tidal ellipse distribution maps between HFR and VMSC_ref.
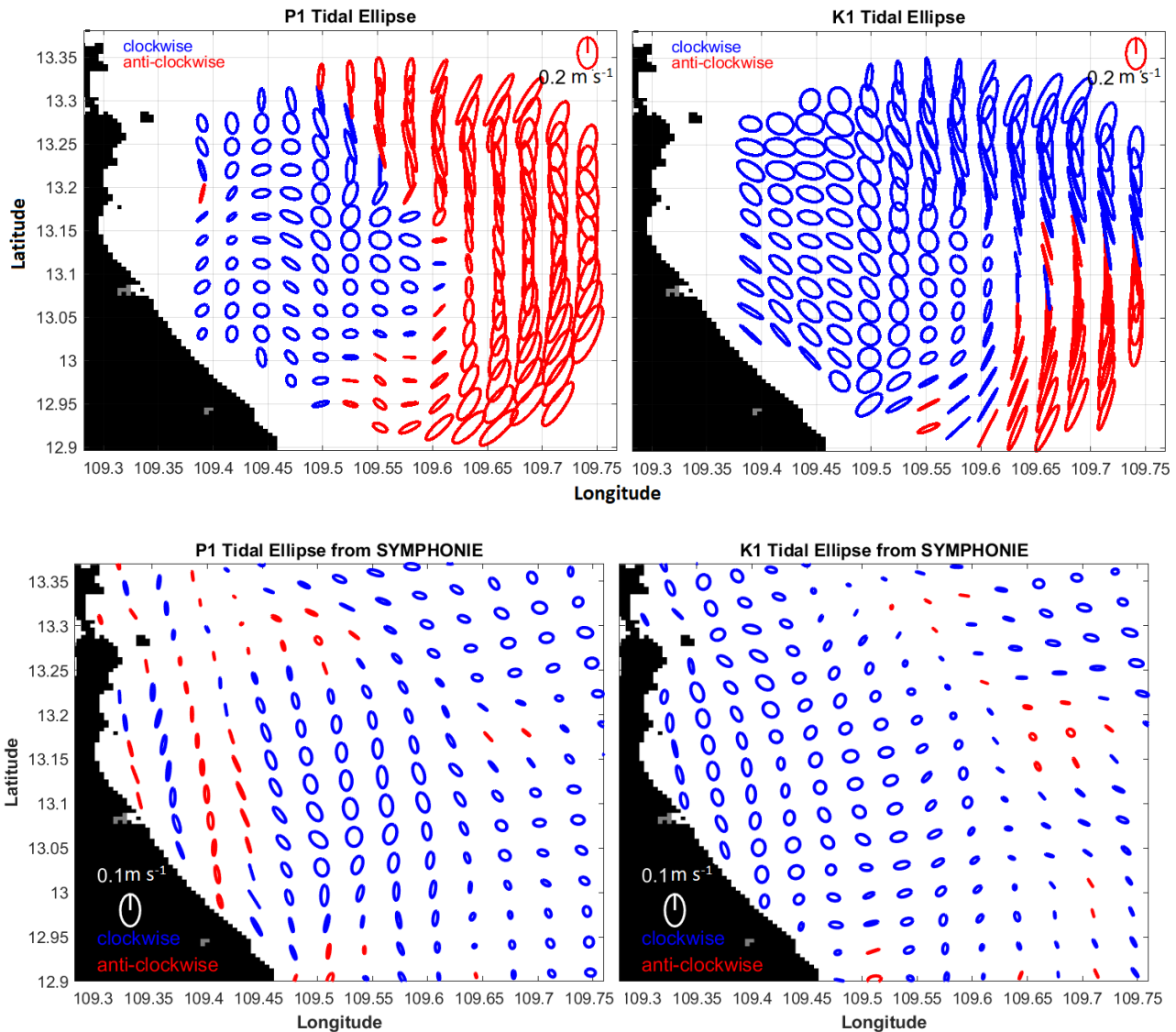
Figure 4: Tidal ellipse distribution for P1 constituent (left) and K1 constituent (right) from HFR (top row) and from VMSC_ref (bottom row)

3.3 SSC variability

Before analysing the results during the analysis period (April-May, 2019), we investigate the variability of SSC field during the same months over the past ten years. SSC during April-May in the years 2009-2018 were simulated by SYMPHONIE for the EASTSEA domain. The 10-year average of the SSC field over these two months is shown in Fig.5a, b. It clearly shows a seaward current occurring within the latitude of 10-14°N. This dynamic feature results in an associated upwelling which starts to form offshore of the VMSC during summer.

11

For the current period of analysis (April-May, 2019), the Fig. 6 shows a remarkable consistency between HFR and EASTSEA run. An intense flow at the southeastern part of the HFR domain has been detected (Fig. 6a, d). This was influenced by the effects of the large-scale South China Sea West Boundary Current (SCSWBC) represented by a strong northeast current. As the monsoon wind changes, the SSC field has a bimodal behavior, where the trace of the SCSWBC in winter (strong current with south-southwest direction) and some features of summer traits (strong jet with eastward-northeastward direction) were both observed in HFR data and well-presented in EASTSEA run, respectively end of April and middle of May (Fig. 6a-b). The weakening of winter SCSWBC together with the strengthening of Southwest monsoon wind caused a seaward flow which were captured in both EASTSEA run and HFR (Fig. 6c). During calm wind conditions, the southward current prevailed over the HFR domain (Fig. 6b). Meanwhile, the currents change the direction to northward and northeastward-eastward direction as southwest wind became stronger (Fig. 6a, c).
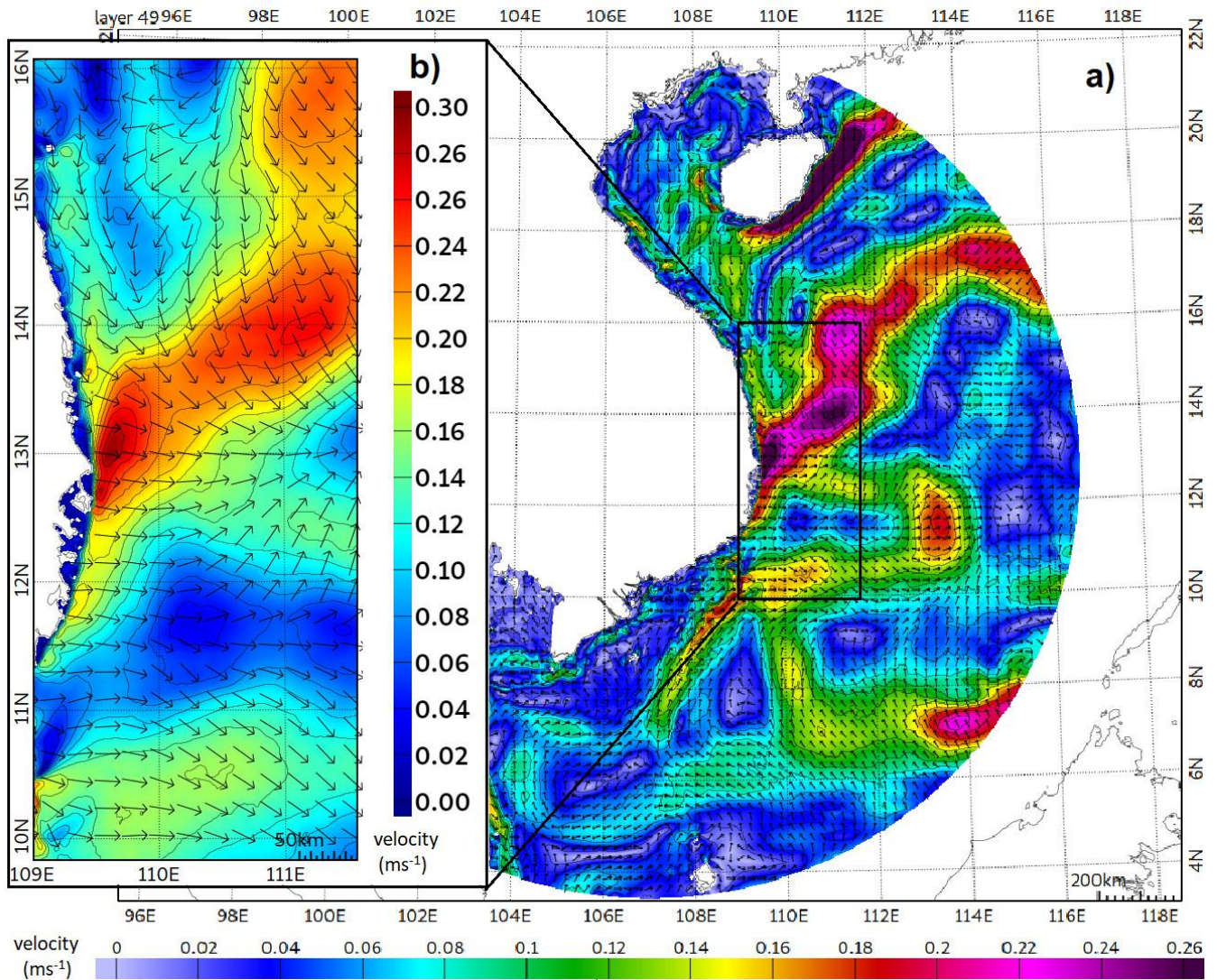
Figure 5: a) Surface circulation in the western SCS in April-May, from the EASTSEA run. The current velocity fields have been averaged for the 10-year period, 2009-2018. b) A zoom-in to the VMSC domain. The colour scale depicts the velocity of surface currents in ms^{-1}. A large upwelling and current separation already occur at latitudes 10-14ºN during this time of the year (Tran et al., 2022)
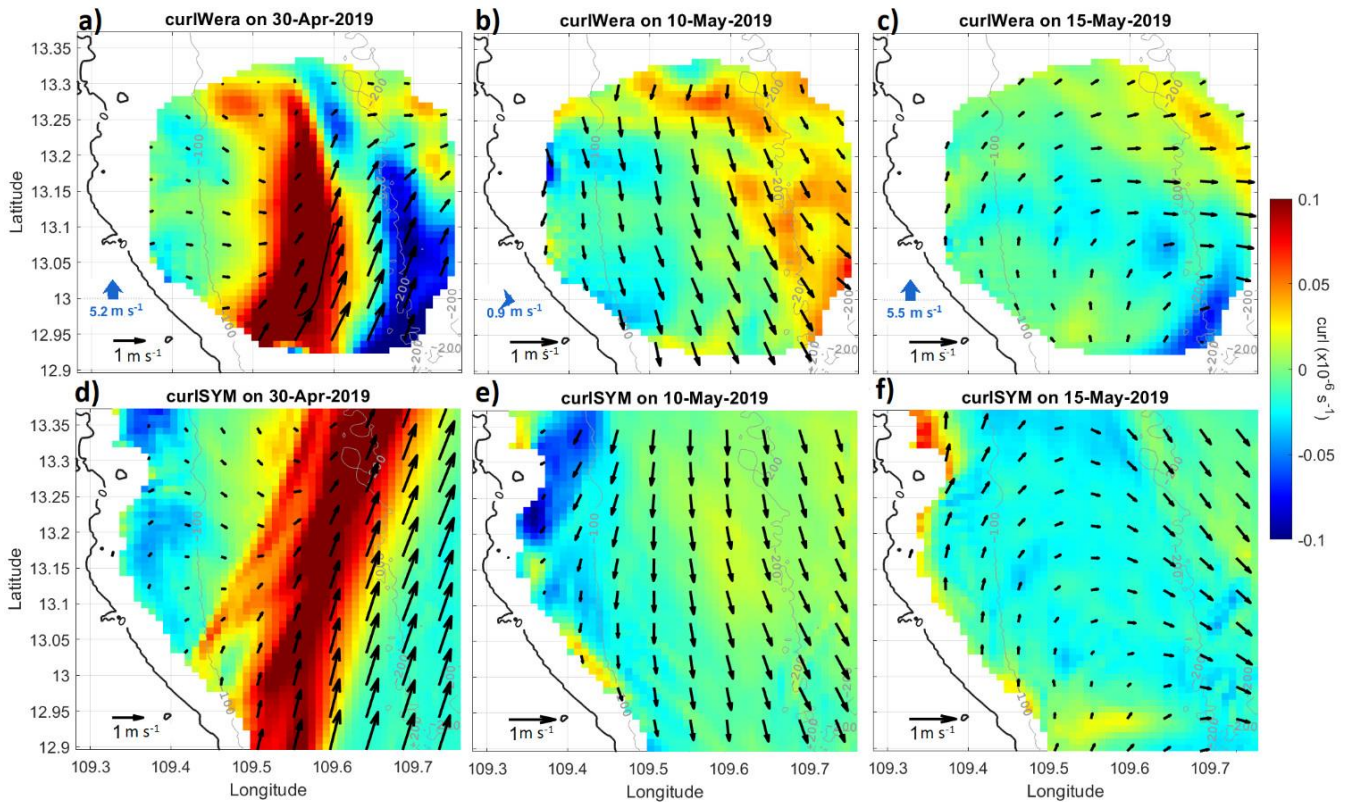
Figure 6: SSC vectors obtained from HFR (a-c) and SYMPHONIE (EASTSEA run) (d-e) superimposing curl of SSC field. Blue arrows in the southwest corner denoted averaged wind directions and magnitudes over the HFR domain. Isobaths are given in gray solid lines, coastlines are represented in black solid lines.

Two different evolutions were observed in both time-series of HFR and the two model runs (EASTSEA and VMSC_ref) (Fig. 7). From the mid-April until the first week of May, strong positive meridional currents were observed in the mid and far fields of the domain, whereas, at the end of the measurement period, the v-component of SSC was inverted to negative and smaller values. This behavior coincides with the evolution of wind time-series, where wind started to change its direction from south-southeast to south-southwest. The magnitudes of SSC v-component are found to be strongly correlated in time with wind. However, a large discrepancy in time-series of v-component of SSC were spotted between EASTSEA, VMSC_ref and HFR at the first 20 days associated with south-southeast wind. During south-southwest wind conditions, the EASTSEA results show better agreement with HFR. In addition, the zonal component of SSC was generally underestimated and the meridional component, on contrary, was overestimated in VMSC_ref and EASTSEA compared to those derived from HFR measurements (Fig. 7a-c). This could come from the uncertainty of the wind forcing input used in the EASTSEA and VMSC_ref, where the impact of local effects is not well described in the global atmospheric models.
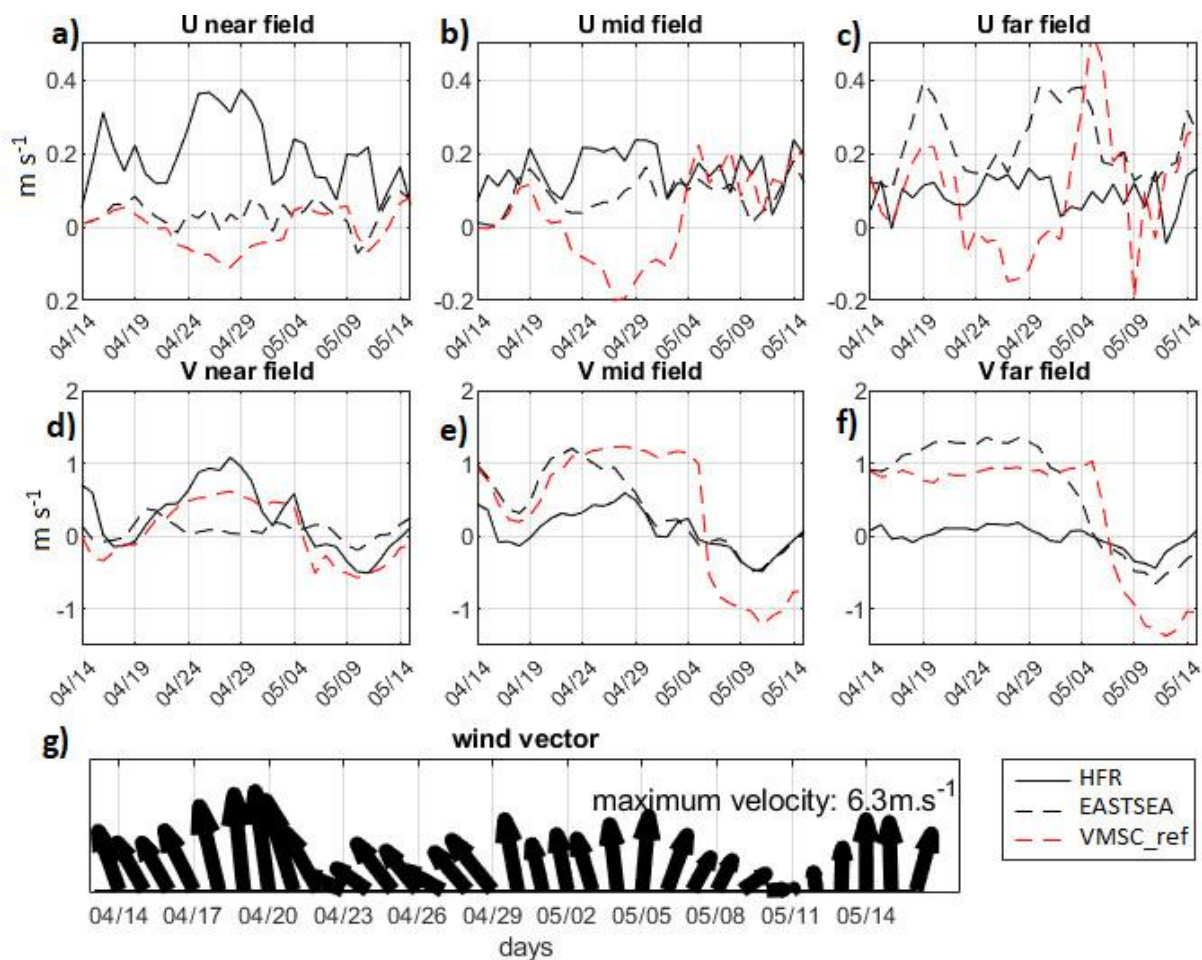
Figure 7: Time-series of u- and v-components of SSC from HFR, EASTSEA and VMSC_ref (a-f); vector time-series of ECMWF wind (g)

The time series of u- and, in particular, v-components of SSC show significant differences between EASTSEA and VMSC_ref despite a similar trend was observed. The two runs started deviating after the third week of April (Fig. 7a-f), associated with a dramatic change in wind direction from strong southern wind to weak eastern wind (Fig. 7g). After the first ten days of May, the u-component of EASTSEA and VMSC_ref show a better agreement, whereas, the VMSC_ref still underestimated the v-component of SSC compared to EASTSEA. The cause for this deviation will be discussed in Sect. 5.

4 Evaluation of modelled surface currents resulting from wind forcing optimization

The SSC velocities from VMSC_ref, VMSC_EkW and VMSC_EnPS are compared with SSC velocities obtained from HFR measurements. The vector difference map in Fig. 8 reveals that the EkW method seems to deliver a better result in vector error

15

reduction in the middle of the domain, as the SSC vector differences in VMSC_EkW (red arrows) are substantially smaller than those in VMSC_EnPS (blue arrows).
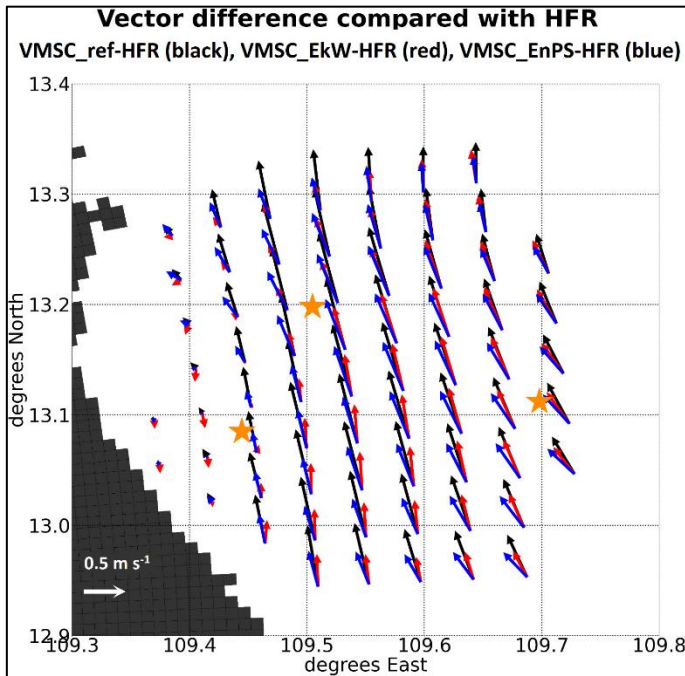

Figure 8: Vector differences of SSC (temporally-averaged over the analysis period) between three simulations compared to HFR measurements: VMSC_ref-HFR (black arrow), VMSC_EkW-HFR (red arrow), VMSC_EnPS-HFR (blue arrow). Locations of three selected points are denoted by orange stars. Vectors were plotted with a three vector point spacing.

In order to evaluate the temporal evolution of velocity fields resulting from different runs (VMSC_ref, VMSC_EnPS and VMSC_EkW) more comprehensively, three points located at near field, mid field and far field of the HFR domain have been selected for comparison (Fig. 9). Besides, three subdomains representing near-, mid- and far fields, where radar measurements were available, were also defined. Near field is limited within 109.3-109.45 degrees East, mid field within 109.45-109.6 degrees East and far field within 109.6-109.75 degrees East.

At near field point, the SSC vectors started rotating from the 2nd day of the period (6th of May, 2019) to the southeast direction and had a similar evolution to that of HFR. Meanwhile, at mid and far field points, the SSC time-series during the first 2-3 days of the analysis period show no significant response to the change of wind fields. This time lag corresponds to the slow adaptation of surface currents to wind forcing.
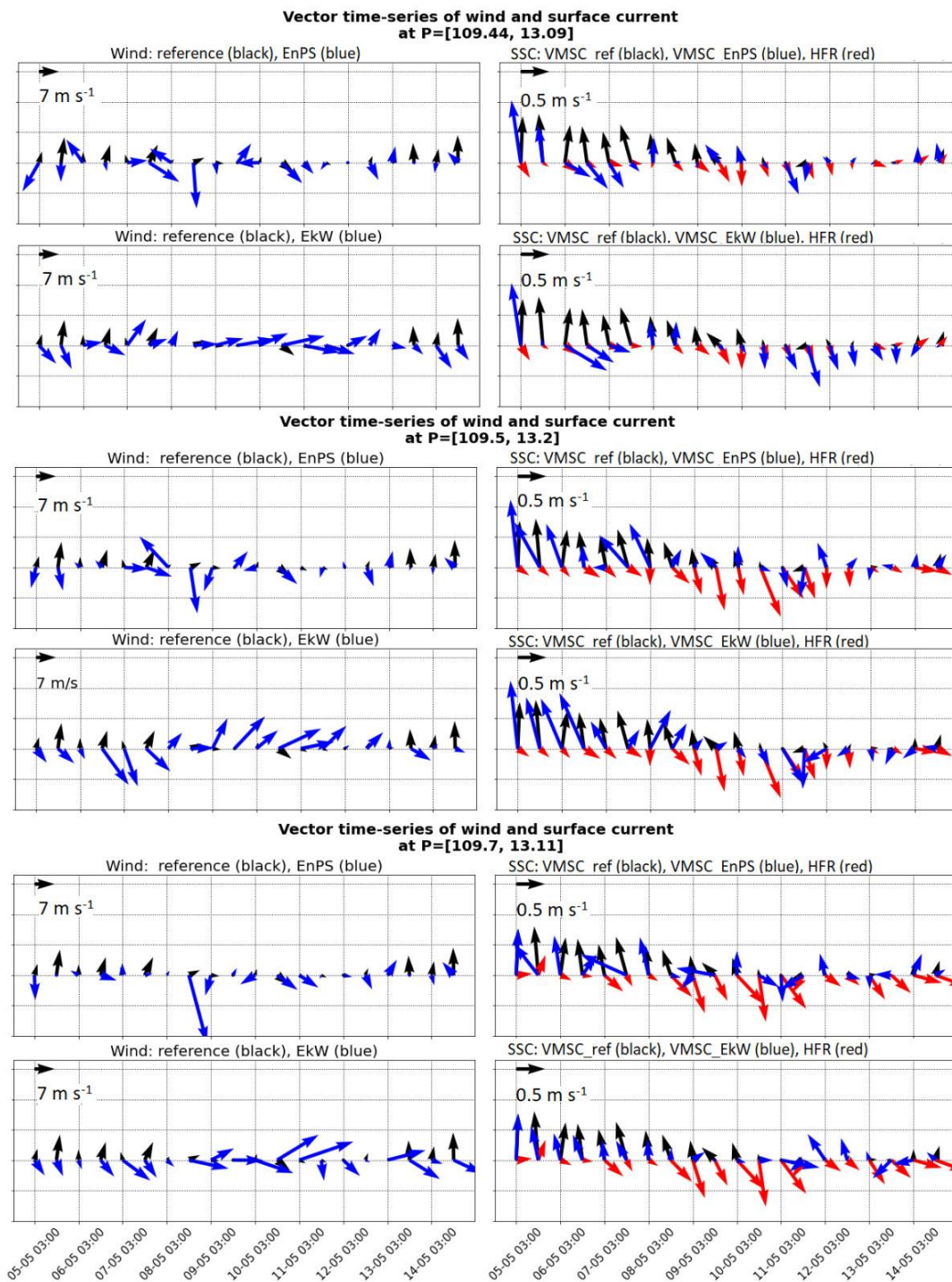
Figure 9: Vector time series of wind (reference, EnPS, EkW) and SSC (VMSC_ref, VMSC_EnPS, VMSC_EkW and HFR) of three points located at near-, mid- and far-field of the HFR domain.

ASCAT wind time-series at near-, mid- and far fields were extracted for comparison with EnPS and EkW winds (Fig. 10). The EnPS wind speed time-series has a better agreement with ASCAT wind compared to that in EkW (Fig. 10a-c). Wind speed at mid and far fields was improved with EnPS method during May 11-13 (Fig. 10b-c) when the wind blew in northward to northeastward direction (Fig. 7g). Figures 10a-c also reveal that the windspeed at the middle of the analysis period (especially during calm wind conditions) is overestimated in EkW method, whereas, EnPS wind speed curves evolved in the similar manner compared to ASCAT. In terms of v-component of wind, EkW seems to achieve better fit to ASCAT at far field (Fig. 10f). The discrepancy between both methods and ASCAT started to increase from May 13 (the grey box on the right of Fig. 10a-f), when the wind speed started to increase considerably (Fig. 7g). The two methods seem to perform well at the middle of the analysis period (May 8-13).
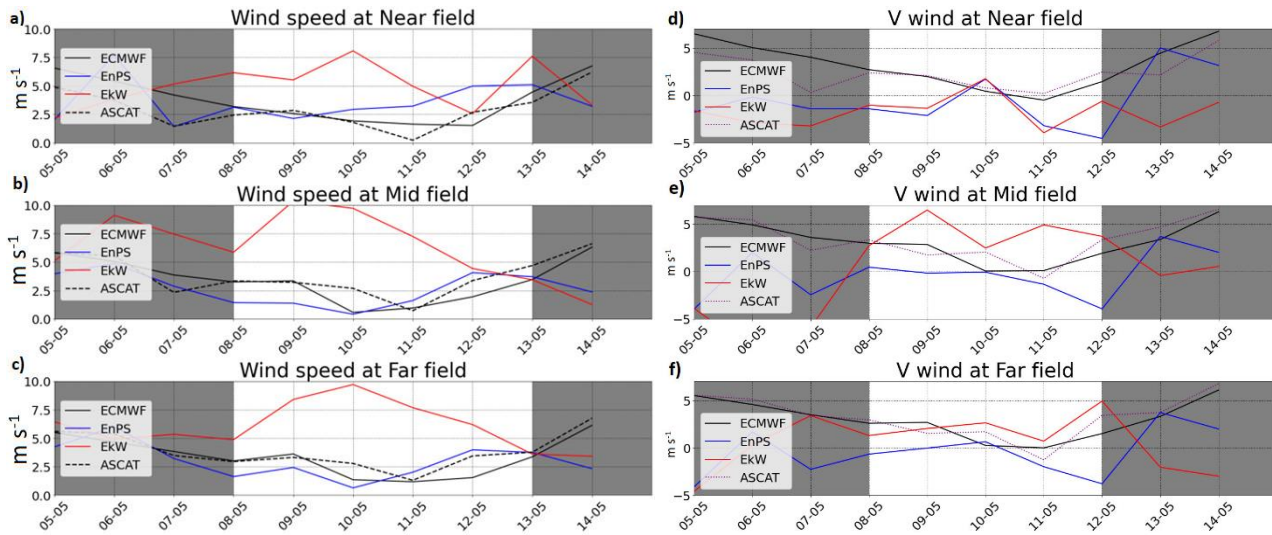

Figure 10: Columns: Wind speed time-series from different wind data (left column); Time series of v-component of wind from wind data (right column); Rows: three sub-domains: near field, mid field and far field

Spatially-averaged RMSEs of surface currents between VMSC_ref, VMSC_EkW and VMSC_EnPS against HFR were calculated for the three subdomains. As a result, the RMSE time-series of u-component of the SSC show no clear improvements from both optimization methods (Fig. 11). Meanwhile, for v-component, the RMSE in VMSC_EkW was reduced significantly (on average, 25 % and 46 % for mid and far fields, respectively) during the analysis period. At the first seven days, the RMSE at near field in VMSC_EkW (dash-line) was found higher than that in the VMSC_ref, however, the RMSE dropped below the reference RMSE line (solid) from the latter days onward. For evaluating the optimization performance between EkW and EnPS methods, spatially-averaged RMSE and MAE for the three subdomains are used as the evaluation metrics and summarized in Table 2. In most cases, EkW and EnPS method errors are reduced compared to the reference run. Both EkW and EnPS are able to mitigate the errors in v-component of SSC significantly, however, only EkW method can achieve the

360 error reduction in u-component of SSC. The subdomain which has the most remarkable improvement after optimization procedure is the mid field (36-46 % of error reduction).
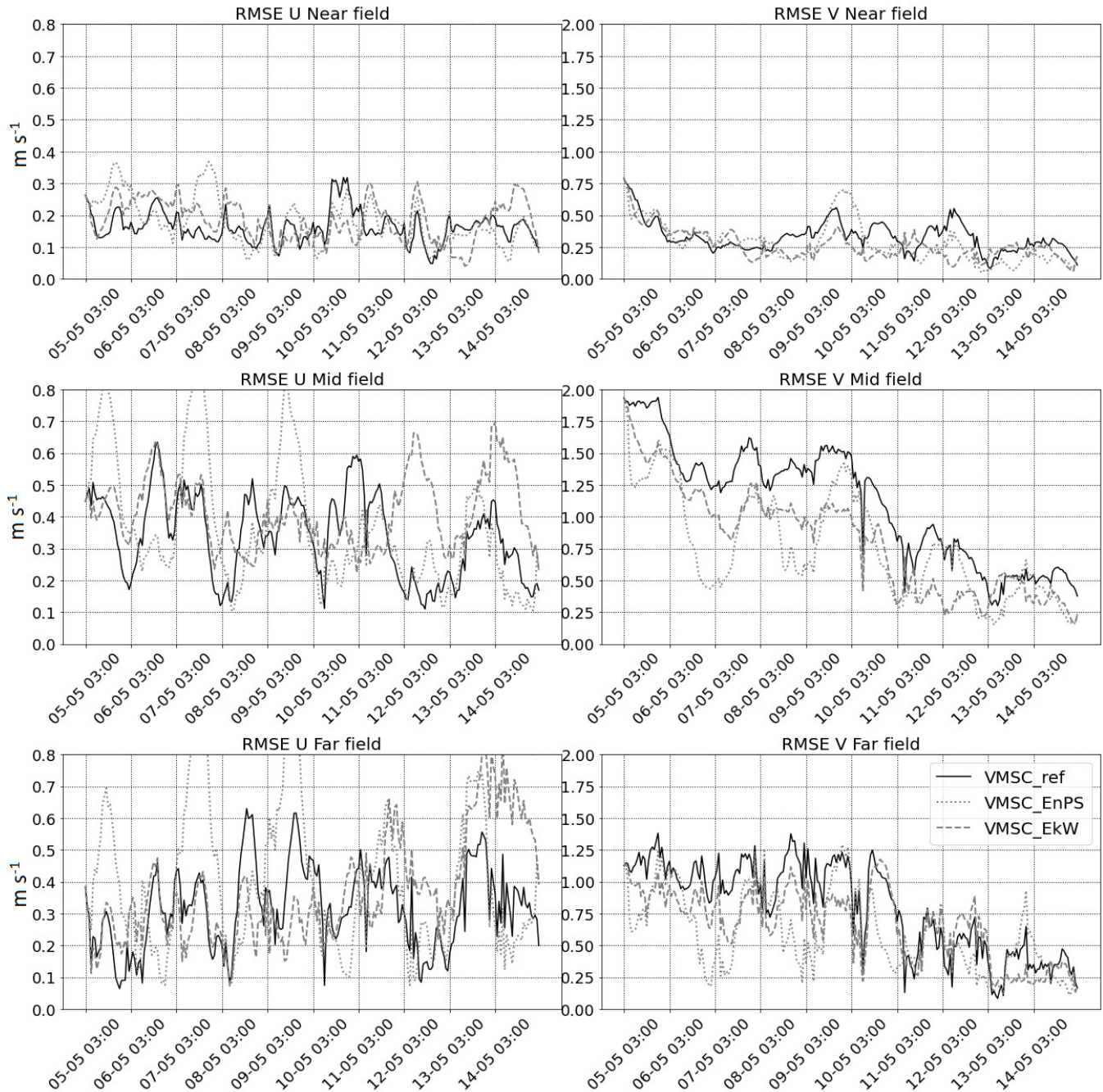

Figure 11: RMSE of u- and v-components of SSC during the analysis period from different simulations, spatially averaged over three subdomains

365

19

Table 2: Time- and space-averaged RMSE and MAE values (in m s^{-1}). Statistics were based on 40 % of measurement data which were not used for optimization procedure

|	U *(m s^{-1})*			V *(m s^{-1})*		
	VMSC_Ref	*VMSC_EnPS*	*VMSC_EkW*	*VMSC_Ref*	*VMSC_EnPS*	*VMSC_EkW*
MAE						
Near field	0.09	0.09	**0.05**	0.19	**0.12**	**0.10**
Mid field	0.17	**0.16**	**0.08**	0.74	**0.46**	**0.38**
Far field	0.20	0.23	**0.17**	0.59	**0.40**	**0.44**
Overall	0.17	0.17	**0.10**	0.58	**0.37**	**0.35**
RMSE						
Near field	0.09	0.11	**0.06**	0.25	**0.16**	**0.12**
Mid field	0.18	0.18	**0.10**	0.74	**0.47**	**0.40**
Far field	0.22	0.24	**0.18**	0.60	**0.41**	**0.45**
Overall	0.18	0.19	**0.13**	0.63	**0.40**	**0.38**

5 Discussion

370   For the first time, high-resolution surface current velocity data were obtained from HFR measurements along the VMSC. The radar coverage represents approx. 4.5 % area of the VMSC domain configured in the model, where the interaction of sea and land as well as other small-scale coastal processes are in place. These processes are typically not well represented in model simulations due to the lack of high-resolution model forcing data and high-resolution bathymetry. The measurements revealed significant differences between model and data, despite temporal evolutions of all time-series (HFR, EASTSEA and VMSC)

375   showed similar trends. Interestingly, surface current velocity fields obtained from EASTSEA and VMSC runs show large variations over time and also a significant difference during some periods of time. This discrepancy could be due to the deviation rising from the forcing propagation at the open boundaries to the smaller-size model domain of computation. In a previous study, in the northwestern Mediterranean Sea, Marmain et al. (2014) have concluded that unexpected features of ocean dynamics could come from a small inconsistency at open boundaries. An additional factor that contributes to this

380   discrepancy is the ocean intrinsic variability (OIV), which operates independently of any change in atmospheric forcing conditions. To support the assumption of an important contribution of OIV to coastal flow variability, we investigated the SSC fields using April-May outputs of the SYMPHONIE ensemble simulations performed by Herrmann et al. (2023) over the EASTSEA domain for the years 2017-2018. A total of ten ensemble simulations were conducted to examine surface currents and upwelling variability off the Vietnamese coast, using the concept of OIV. To generate ensembles, small-scale perturbations

385   were introduced in the model initial fields without disturbing the whole forcing data (see Herrmann et al. 2023 for details). Subsequently, the SSC data obtained from these ensemble runs were used to calculate the OIV index and the monthly mean standard deviation of ensemble vorticity ($\bar{\sigma}_v$) from SSC field in April-May, 2017-2018. The OIV index, explained in Herrmann

et al. 2023, is the ratio between the ensemble standard deviation and the ensemble mean of the temporal average over a given period of time of surface currents. It quantifies the contribution of OIV to SSC variability over the selected period, April-May, 2017-2018. The analysis of model outputs showed that high values of $\bar{\sigma}_v$ are found near the coasts of the HFR domain, revealing large fluctuations within the ensembles induced by OIV (Fig. 12a-d). In terms of OIV index, high values (OIV>10) are observed near the coasts, in particular around 15 km offshore along 12.9-13.1° N, associated with the specific feature of the coastal circulation, i.e. northeastern current jet (Fig. 12e). This result emphasizes that the SSC variability in our study region is significantly influenced by OIV, regardless of external forcing. Similar conclusions and relevant discussions have been raised in previous studies for this region under different names, such as the North Coastal Upwelling (Ngo and Hsin, 2021; To Duy et al., 2022), South Vietnam Upwelling (Da, 2018), Vietnamese coasts (Metzger, 2003).
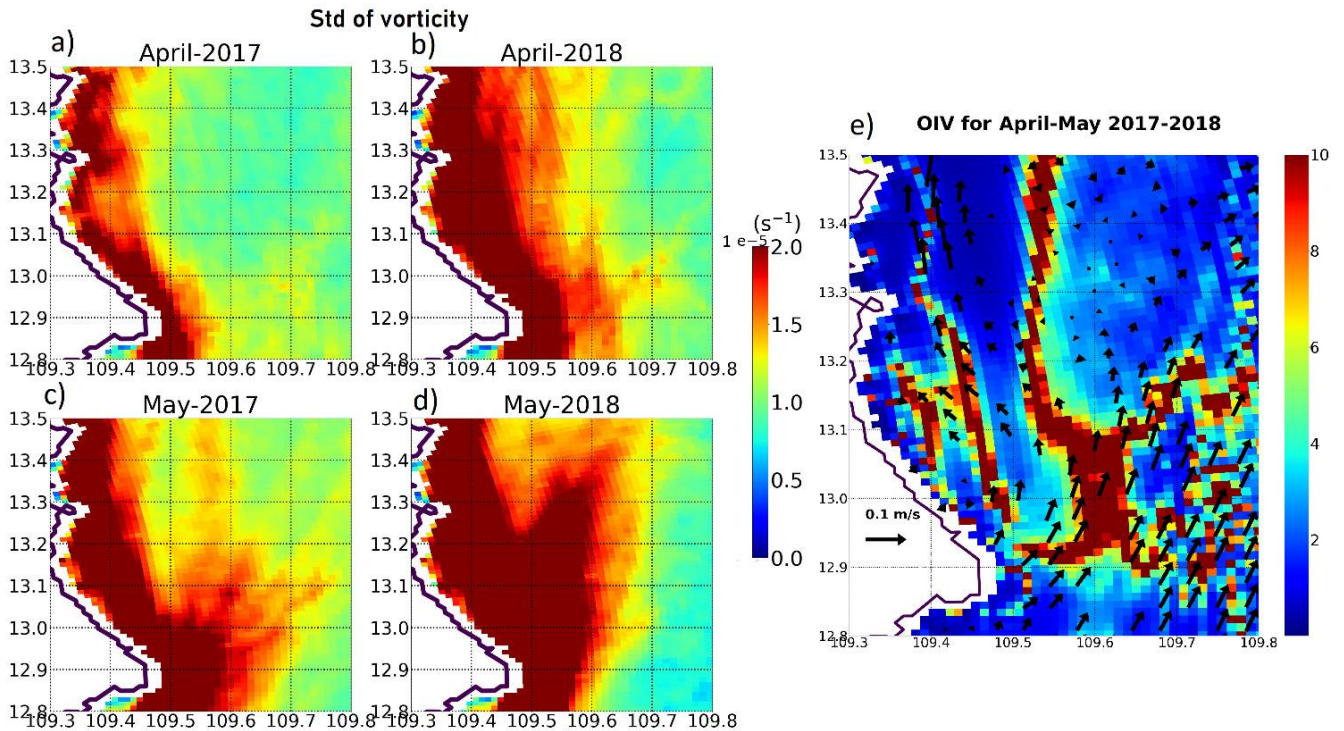
Figure 12: (a-d) Monthly mean standard deviation of SSC vorticity over ensembles; e) OIV index superimposed with multi-annual monthly average SSC vectors for April-May, 2017-2018

The study results above highlight that, winds play an important role in the variability of coastal surface currents in the VMSC at small temporal and spatial scales. Different wind forcing conditions using in different model simulations (VMSC_ref, VMSC_EkW, and VMSC_EnPS) yielded notably different SSC fields at 1 km resolution during a short time of analysis (May 5-14, 2019). As illustrated in Fig. 9e-f, opposite directions of SSC vectors between HFR and VMSC_ref were observed, which indicates that no northeast current occurred in the HFR domain during the time of analysis, whereas, this strong northeast jet

presented clearly in VMSC_ref simulation. Previous studies also pointed out that Ekman transport associated with winds can modify the position of the northeast jet and upwelling at the latitudes 12-14°N (Metzger, 2003; Shaw and Chao, 1994). Besides, De Gaetano et al. (2010) has confirmed the great impacts of different resolutions of wind on the inshore features of surface

410 circulations, especially small-scale processes i.e. sub-mesoscale eddy formation. Thus, the limitation of grid resolution of the global atmospheric model can cause the incapability in capturing the local effects on wind field i.e. orographic effects induced by complex terrains, and the coastal wind variability during the monsoon transition period. In this particular case, two mountain ranges and a cape in the south of the domain (Fig. 1c) form a 'corridor' for winds to blow seaward in cross-shelf direction. The increase of surface heat at a valley between two mountains causes high convection and convergence zone at the coasts

415 (Bei et al., 2018). Furthermore, when the activity of larger-scale winds is weak, this phenomenon becomes dominant. Counting the high wind variation during transition period, the behavior of coastal winds become more complex and cannot be resolved at grid-scale of global models. Previously, a warning has been given in Metzger (2003) when using the ECMWF wind product in coastal model as spurious wind stress curls along the coastal boundaries, especially in regions with a complex orography, could reproduce misleading small-scale circulation along the coasts. Another point to be discussed is a poor availability of

420 independent observed wind data for the coastal regions in Vietnam. There are two meteorological stations located in the vicinity of the study area. A comparison was conducted between wind time-series data from these two meteorological stations and wind data from the ECMWF, EkW, and EnPS during the analysis period. The resulting correlations were found to be relatively low (less than 0.3) due to their distance inland from the coastline (10 and 15km), indicating that the data are not representative of winds in the open sea. In contrast, the ASCAT wind data used for validation has a very coarse resolution (0.25 degree ~ 25

425 km) assumed to be insufficient for representing the wind field close to the coastlines. The comparison between model runs and ASCAT data in Fig. 10 already shows that the behaviors of winds amongst different wind time-series are more comparable at far field, where the land morphology and orography no longer have impacts on coastal dynamics.

The EnPS and EkW methods have been applied to different periods (both April and May) but only the period from May 5 to May 14 was selected for analysis. During this period, the current velocity maps from HFR demonstrated large variability of

430 circulation patterns (Fig. 6a,b,c), which were not consistent with the evolution of the ECMWF wind. Furthermore, a significant discrepancy was observed between the model and observations in v-component of the surface currents accompanied by a considerable change in wind direction (Fig. 7e,f,g). In light of these evidences, our hypothesis was that wind forcing was the primary source of errors in model simulations. However, the optimization results showed that both methods exhibited limitations in producing an optimal wind field for the entire analysis period. At mid field and far field, the EnPS method

435 achieved better wind field compared to ECMWF wind data however large discrepancies still occurred during the period when the ECMWF showed good agreements with ASCAT winds. This could be explained by the fact that nearshore circulations (the first ~30 km offshore) are not only governed by winds but other processes, as explained above. Besides, the optimization methods performed better during southern and southwestern winds, and is sensitive to the change in wind direction and when wind speed is weak. This constraint could be due to the insufficient number of ensembles used in EnPS method. In this research,

440 only a cluster of 50 wind forcing ensemble members were used while Barth et al. (2011) used 100 wind ensemble members

22

for correcting the model surface currents to obtain good statistics for calculating covariances. In case of EkW method, a constant drag coefficient was used instead of wind-dependent one. The sensitivity to the drag coefficient variation has not yet been tested.

6 Conclusion and future work

445 The coastal dynamics of the VMSC, especially within the HFR measurement domain, during the transition period of summer monsoon is influenced by various factors, amongst others, winds, coastal topography, and larger-scale background circulation variability. Compared to SSC obtained from HFR measurements, SYMPHONIE model is capable to characterize the coastal circulation variability as it could capture relatively well the spatial patterns of SSC. However, a large discrepancy in velocity time series between model and HFR are found in April associated with the eastern and southeastern winds. This is a limitation 450 of model in simulating coastal circulation under complex variation of wind.

The EnPS and EkW methods show improvements in v-component of SSC as RMSE and MAE reduced remarkably (36-40 %), whereas, there is no significant improvements in u-component. The bottleneck of this study is there are no nearby offshore wind stations or wind measurements during the HFR measurement period for validation. Wind data records at two nearest meteorological stations are not representative as the stations are located inland far from the shore. The ASCAT wind data used 455 for validation have a very coarse resolution thus cannot describe the wind behavior due to orographic effects close to the coasts. Therefore, a comprehensive measurement campaign including wind measurements should be considered in the next step of our future work on the region.

Although the overall discrepancies were reduced by ~40 %, a good agreement between the SSC time-series obtained from HFR measurements and from wind-optimized model runs is still not yet established. Especially during calm wind conditions, 460 strong southeastward current velocities still presented all over the HFR domain. This phenomenon could be governed by different processes, for instance, the background circulation at larger scales from outside of the VMSC domain. Thus, wind optimization alone is not capable to deliver a sufficient improvement in simulation results of surface currents. For this reason, OBC optimization should be tested in the next step of our study with an expectation to obtain a better model simulation of the coastal dynamical processes in the VMSC region.

465 Last but not least, the optimisation results revealed that the surface circulation is influenced not only by winds but also by other factors such as intrinsic ocean variability which is not entirely controlled by boundary conditions. Another factor which contributes to the variability of the velocity field within the study region could be the interaction of a powerful flow with headlands: the cape located in the south of the domain produces small-scale features of circulation, i.e. eddies. This indicates the potential usefulness of large velocity datasets, amongst others, an adequate monitoring network with good coverage and 470 temporal resolution, i.e., HFR systems, and other data fusion methods to effectively improve modelling results in such highly-dynamic regions.

23

7 Appendix

Figure A1 shows accuracy values which were extracted from standard WERA Data Viewer provided by the HFR manufacturer. Higher uncertainties of both u- and v-components of SSC from HFR measurements are found in the offshore range starting
475 from a distance of ~40 km. The high values (high noise level) are associated with the occurrence of 50 Hz noise band and its harmonics caused by electrical power supply in the surrounding areas of WERA locations. Spurious radial currents are the results of the smeared-out signal of noise with the first-order peaks (which give the information of radial currents) in the Doppler spectra. Although most of spikes in original HFR data have been removed, the noise still contaminated some parts of the domain, in particular at range more than 40 km, where 50 Hz-harmonic noise bands are present.

480
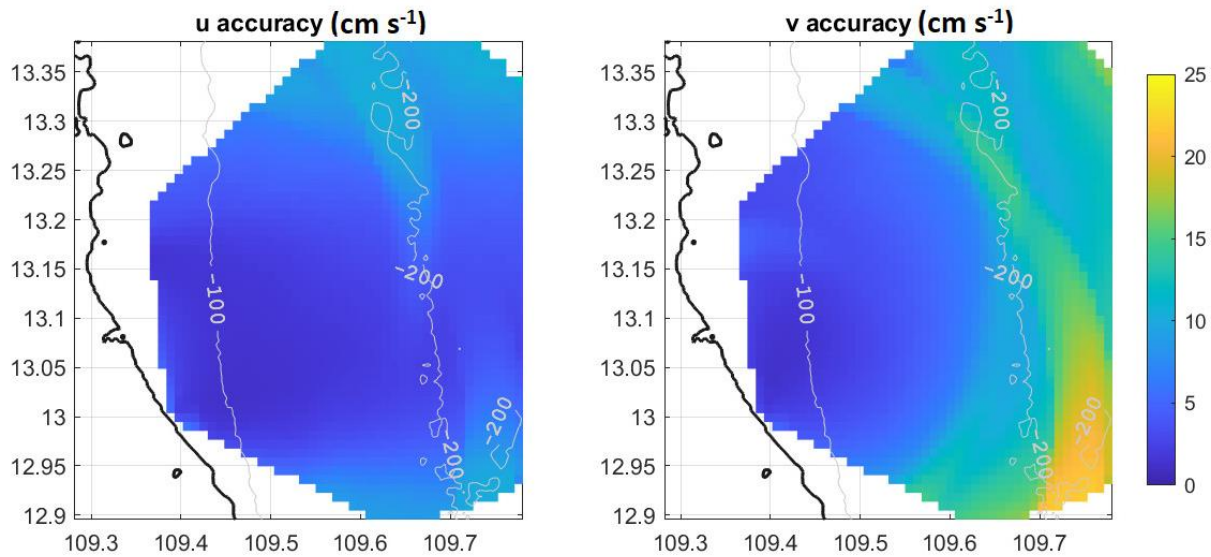
Figure A1: Mean accuracy map of u- and v-components of sea surface currents from HFR measurements for the entire period of measurements.

Code and data availability

485 The SYMPHONIE model can be downloaded free-of-charge from https://sirocco.obs-mip.fr/ocean-models/s-model/download/ and is presented in Marsaleix et al. (2008). Atmospheric forcing data and ocean data used as initial ocean conditions and lateral ocean boundary conditions are available on https://10.5281/zenodo.13253326.

Measurement data (HFR and AWAC) should be requested from CEFD-HUS/VNU and cannot be provided by the authors.

The code of optimization methods can be provided upon request.

References

505 Barth, A., Alvera-Azcárate, A., Beckers, J. M., Weisberg, R. H., Vandenbulcke, L., Lenartz, F., and Rixen, M.: Dynamically constrained ensemble perturbations - Application to tides on theWest Florida Shelf, Ocean Sci., 5, 259–270, https://doi.org/10.5194/os-5-259-2009, 2009.

Barth, A., Alvera-Azcárate, A., Beckers, J. M., Staneva, J., Stanev, E. V., and Schulz-Stellenfleth, J.: Correcting surface winds by assimilating high-frequency radar surface currents in the German Bight, Ocean Dyn., 61, 599–610,
510 https://doi.org/10.1007/s10236-010-0369-0, 2011.

Bei, N., Zhao, L., Wu, J., Li, X., Feng, T., and Li, G.: Impacts of sea-land and mountain-valley circulations on the air pollution in Beijing-Tianjin-Hebei (BTH): A case study, Environ. Pollut., 234, 429–438, https://doi.org/10.1016/j.envpol.2017.11.066, 2018.

Centurioni, L. R., Niiler, P. N., and Lee, D. K.: Near-surface circulation in the South China Sea during the winter monsoon,
515 Geophys. Res. Lett., 36, 1–6, https://doi.org/10.1029/2008GL037076, 2009.

Chen, C., Lai, Z., Beardsley, R. C., Xu, Q., Lin, H., and Viet, N. T.: Current separation and upwelling over the southeast shelf

of Vietnam in the South China Sea, J. Geophys. Res. Ocean., 117, 1–16, https://doi.org/10.1029/2011JC007150, 2012.

Codiga, D. L.: Unified tidal analysis and prediction using the UTide Matlab functions, echnical Report 2011-01., Narragansett, RI, 59 pp., https://doi.org/10.13140/RG.2.1.3761.2008, 2011.

520 Cosoli, S., Ličer, M., Vodopivec, M., and Malačič, V.: Surface circulation in the Gulf of Trieste (northern Adriatic Sea) from radar, model, and ADCP comparisons, J. Geophys. Res. Ocean., 118, 6183–6200, https://doi.org/10.1002/2013JC009261, 2013.

Cosoli, S., Pattiaratchi, C., and Hetzel, Y.: High-Frequency Radar Observations of Surface Circulation Features along the South-Western Australian Coast, J. Mar. Sci. Eng., 8, 97, https://doi.org/10.3390/jmse8020097, 2020.

525 Da, N. D.: The interannual variability of the South Vietnam Upwelling : contributions of atmospheric, oceanic, hydrologic forcing and the ocean intrinsic variability , 1–168, 2018.

Da, N. D., Herrmann, M., Morrow, R., Niño, F., Huan, N. M., and Trinh, N. Q.: Contributions of Wind, Ocean Intrinsic Variability, and ENSO to the Interannual Variability of the South Vietnam Upwelling: A Modeling Study, J. Geophys. Res. Ocean., 124, 6545–6574, https://doi.org/10.1029/2018JC014647, 2019.

530 David S-K. Ting: Wall Turbulence, in: Basics of Engineering Turbulence, edited by: David S-K. Ting, Elsevier Inc., 119–138, https://doi.org/https://doi.org/10.1016/C2015-0-00322-7, 2016.

Duy, T. T., Herrmann, M., Estournel, C., Marsaleix, P., Duhaut, T., Hong, L. B., and Bich, N. T.: Role of wind , mesoscale dynamics and coastal circulation in the interannual variability of South Vietnam Upwelling , South China Sea . Answers from a high resolution ocean model, 1–34, 2022.

535 Estournel C., Auclair F, Lux M., Nguyen C., M. P.: "Scale oriented" embedded modeling of the North-Western Mediterranean in the frame of MFSTEP, Ocean Sci., 5, 73–90, 2009.

Fang, G., Wang, G., Fang, Y., and Fang, W.: A review on the South China Sea western boundary current, Acta Oceanol. Sin., 31, 1–10, https://doi.org/10.1007/s13131-012-0231-y, 2012.

De Gaetano, P., Burlando, M., Doglioli, A. M., and Petrenko, A. A.: Wind forcing effects on coastal circulation Wind forcing
540 effects on coastal circulation and eddy formation around a cape Wind forcing effects on coastal circulation, Ocean Sci. Discuss, 7, 207–249, 2010.

Gu, H. and Mao, Y.: Multi-Timescale Characteristics of Southwestern Australia Nearshore Surface Current and Its Response

to ENSO Revealed by High-Frequency Radar, Remote Sens., 16, 209, https://doi.org/10.3390/rs16010209, 2024.

Herrmann, M. and To Duy, T.: Mechanisms and intraseasonal variability of the South Vietnam Upwelling, South China Sea:
545   role of circulation, tides and rivers., Ocean Sci., https://doi.org/https://doi.org/10.5194/egusphere-2024-368, 2024.

Herrmann, M., To Duy, T., and Estournel, C.: Intraseasonal variability of the South Vietnam upwelling, South China Sea:
influence of atmospheric forcing and ocean intrinsic variability, Ocean Sci., 19, 453–467, https://doi.org/10.5194/os-19-453-
2023, 2023.

J. T. Potemra and T. Qu: Ocean currents -The Oceans: The Parcific Ocean, in: Nature, vol. 3, 117–118,
550   https://doi.org/10.1038/003469a0, 2009.

Lauton, G., Marta-Almeida, M., and Lentini, C. A. D.: The Effect of Currents on Large Surface Gravity Waves Under Cyclonic
Conditions in the South/Southeastern Brazil, J. Geophys. Res. Ocean., 128, 1–16, https://doi.org/10.1029/2022JC018472,
2023.

Li, Y., Han, W., Wilkin, J. L., Zhang, W. G., Arango, H., Zavala-Garay, J., Levin, J., and Castruccio, F. S.: Interannual
555   variability of the surface summertime eastward jet in the South China Sea, J. Geophys. Res. Ocean., 119, 7205–7228,
https://doi.org/10.1002/2014JC010206, 2014.

Mantovani, C., Corgnati, L., Horstmann, J., Rubio, A., Reyes, E., Quentin, C., Cosoli, S., Asensio, J. L., Mader, J., and Griffa,
A.: Best Practices on High Frequency Radar Deployment and Operation for Ocean Current Measurement, Front. Mar. Sci., 7,
1–21, https://doi.org/10.3389/fmars.2020.00210, 2020.

560   Marmain, J., Molcard, A., Forget, P., Barth, A., and Ourmieres, Y.: Assimilation of hf radar surface currents to optimize
forcing in the northwestern mediterranean sea, Nonlinear Process. Geophys., 21, 659–675, https://doi.org/10.5194/npg-21-
659-2014, 2014.

Marsaleix, P., Auclair, F., Floor, J. W., Herrmann, M. J., Estournel, C., Pairaud, I., and Ulses, C.: Energy conservation issues
in sigma-coordinate free-surface ocean models, Ocean Model., 20, 61–89, https://doi.org/10.1016/j.ocemod.2007.07.005,
565   2008.

Metzger, E. J.: Upper ocean sensitivity to wind forcing in the South China Sea, J. Oceanogr., 59, 783–798,
https://doi.org/10.1023/B:JOCE.0000009570.41358.c5, 2003.

Ngo, M. H. and Hsin, Y. C.: Impacts of Wind and Current on the Interannual Variation of the Summertime Upwelling Off
Southern Vietnam in the South China Sea, J. Geophys. Res. Ocean., 126, 1–23, https://doi.org/10.1029/2020JC016892, 2021.

570   Nguyen-Duy, T., Ayoub, N. K., De-Mey-Frémaux, P., and Ngo-Duc, T.: How sensitive is a simulated river plume to uncertainties in wind forcing? A case study for the Red River plume (Vietnam), Ocean Model., 186, 102256, https://doi.org/10.1016/j.ocemod.2023.102256, 2023.

Nguyen, D. T.: Variability of the Red River plume in the Gulf of Tonkin from stochastic modeling and cluster analysis. Ocean, Atmosphere., Université Paul Sabatier - Toulouse III, 2022, 2022.

575   Rogowski, P., Zavala-Garay, J., Shearman, K., Terrill, E., Wilkin, J., and Lam, T. H.: Air-Sea-Land Forcing in the Gulf of Tonkin: Assessing Seasonal Variability Using Modern Tools, Oceanography, 32, 150–161, https://doi.org/10.5670/oceanog.2019.223, 2019.

Sentchev, A., Forget, P., Barbin, Y., and Yaremchuk, M.: Surface circulation in the Iroise Sea (W. Brittany) from high resolution HF radar mapping, J. Mar. Syst., 109–110, S153–S168, https://doi.org/10.1016/j.jmarsys.2011.11.024, 2013.

580   Shaw, P. T. and Chao, S. Y.: Surface circulation in the South China Sea, Deep. Res. Part I, 41, 1663–1683, https://doi.org/10.1016/0967-0637(94)90067-1, 1994.

Sim, S. K., Peinke, J., and Maass, P.: Signatures of geostrophic turbulence in power spectra and third - order structure function of offshore wind speed fluctuations, Sci. Rep., 1–10, https://doi.org/10.1038/s41598-023-40450-9, 2023.

To Duy, T., Herrmann, M., Estournel, C., Marsaleix, P., Duhaut, T., Bui Hong, L., and Trinh Bich, N.: The role of wind,
585   mesoscale dynamics, and coastal circulation in the interannual variability of the South Vietnam Upwelling, South China Sea - answers from a high-resolution ocean model, Ocean Sci., 18, 1131–1161, https://doi.org/10.5194/os-18-1131-2022, 2022.

Tran, M. C., Sentchev, A., Berti, S., Ayoub, N. K., Nguyen-Duy, T., and Cuong, N. K.: Assessment of relative dispersion in the Gulf of Tonkin using numerical modeling and HF radar observations of surface currents, Cont. Shelf Res., 245, 104784, https://doi.org/10.1016/j.csr.2022.104784, 2022a.

590   Tran, T. H., Sentchev, A., Tran, M. C., Duc Dang, D., and Helzel, T.: Assessments of surface current variability along the mid-southern coast of Vietnam from high-frequency (HF) radar measurements, in: OCEANS 2022 - Chennai, 1–5, https://doi.org/10.1109/OCEANSChennai45887.2022.9775414, 2022b.

Tran, T. H., To, D. T., and Sentchev, A.: Coastal dynamics in middle-south Vietnam during a transition period of Asian monsoon , characterized by HF radar measurements and numerical modeling, 0–2, 2023.

595   Trinh, N. B., Herrmann, M., Ulses, C., Marsaleix, P., Duhaut, T., To Duy, T., Estournel, C., and Shearman, R. K.: New insights into the South China Sea throughflow and water budget seasonal cycle: evaluation and analysis of a high-resolution

configuration of the ocean model SYMPHONIE version 2.4, Geosci. Model Dev., 17, 1831–1867, https://doi.org/10.5194/gmd-17-1831-2024, 2024.

Wang, G., Chen, D., and Su, J.: Generation and life cycle of the dipole in the South China Sea summer circulation, J. Geophys. Res. Ocean., 111, https://doi.org/10.1029/2005JC003314, 2006.

Wang, L., Chen, H., Chowdary, J. S., Ha, K.-J., Kajikawa, Y., and Martin, G.: Editorial: The Asian Monsoon, Front. Earth Sci., 9, https://doi.org/10.3389/feart.2021.748811, 2021.

Weber, J. E.: Steady Wind- and Wave-Induced Currents in the Open Ocean, Phys. Oceanogr., 13, 524–530, 1983.

Wu, Y., Tang, Q., Chen, Z., Liu, Y., and Zhou, C.: Diurnal and Seasonal Variation of High-Frequency Gravity Waves at Mohe and Wuhan, Atmosphere (Basel)., 13, https://doi.org/10.3390/atmos13071069, 2022.

Yang, Z., Wang, G., and Chen, C.: Horizontal velocity structure of mesoscale eddies in the South China Sea, Deep. Res. Part I Oceanogr. Res. Pap., 149, 103055, https://doi.org/10.1016/j.dsr.2019.06.001, 2019.

Yaremchuk, M. and Sentchev, A.: Mapping radar-derived sea surface currents with a variational method, Cont. Shelf Res., 29, 1711–1722, https://doi.org/10.1016/j.csr.2009.05.016, 2009.

Yaremchuk, M. and Sentchev, A.: A combined EOF/variational approach for mapping radar-derived sea surface currents, Cont. Shelf Res., 31, 758–768, https://doi.org/10.1016/j.csr.2011.01.009, 2011.

Zhou, H., Yuan, D., Li, R., and He, L.: The western South China Sea currents from measurements by Argo profiling floats during October to December 2007, Chinese J. Oceanol. Limnol., 28, 398–406, https://doi.org/10.1007/s00343-010-9052-z, 2010.